THE JOURNAL OF PHYSICAL CHEMISTRY C
A JOURNAL OF THE AMERICAN CHEMICAL SOCIETY

pubs.acs.org/JPCC
Article

Mechanistic Diversity in the Hydrolysis of Sarin by Single Transition-Metal Atoms on MOF-808

Carl Fossum and Diego Troya*

Cite This: J. Phys. Chem. C 2024, 128, 8983−8992
Read Online

ACCESS | Metrics & More | Article Recommendations | Supporting Information

ABSTRACT: Zr-based metal−organic frameworks (Zr-MOFs) are one of the most promising materials for the decomposition of chemical warfare nerve agents. We present a study of the hydrolysis reaction mechanism of nerve agent sarin catalyzed by Zn(II) and Ti(IV) single atoms on the Zr-MOF MOF-808. We reveal that upon binding of the nerve agent to the catalyst, conformational isomerism leads to a great diversity of hydrolysis reaction mechanisms. Each mechanism follows an addition−elimination sequence but differs markedly in the way the elimination step is accomplished and its energetics. Moreover, while most of the prior work has focused on the HF elimination channel, this work shows that the addition−elimination steps can also lead to isopropanol formation through barriers comparable to those of the HF channel. Additional insight is achieved by high-level electronic structure calculations, including coupled-cluster theory, which allow us to benchmark more efficient DFT techniques commonly used in mechanistic studies of catalytic processes involving transition-metal atoms. Overall, this work reveals new reaction pathways for nerve-agent hydrolysis with lower-lying transition-state energies than previously reported, highlighting the importance of conformational sampling in mechanistic studies of catalytic processes.

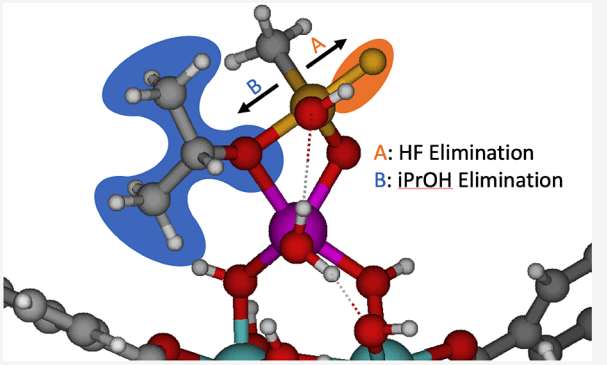

INTRODUCTION

Organophosphonate chemical warfare agents (CWAs) constitute some of the most biologically toxic compounds ever mass-produced for wartime use.[1−3] Despite international efforts to both limit proliferation and promote the disarmament of CWA stockpiles, recent use by terrorist organizations and governments alike indicates additional measures need to be taken to protect human life.[4−7] With current decontamination and personal protective equipment proving to be of limited efficacy, there is continued interest in developing the next generation of CWA decontamination methods.[8] In recent years, Zirconium-based metal−organic frameworks (Zr-MOFs) have proven to be one of the most promising materials for the degradation of nerve agents (NAs).[9−14] A select set of Zr-MOFs is capable of hydrolysis of NAs with half-lives below 1 min in buffered solution.[10,12] Immense focus has been placed on three Zr-MOFs of identical secondary-building unit (SBU), Zr_6 $(\mu_3{-}O)_4(\mu_3{-}OH)_4$, but different connectivity: UiO-66 (12-connected),[15] NU-1000[16] (8-connected), and MOF-808 (6-connected).[17] MOF-808 exhibits the largest hydrolysis rate, implying that for identical SBUs, reduced connectivity improves the availability of active Zr(IV) sites at the SBU.[12,14]

While the solution hydrolysis of nerve agents with Zr-MOFs is impressively fast, product inhibition has been shown in buffered solution,[14] unbuffered solution,[18] and at the gas−surface interface.[19,20] Spectroscopic characterization of Zr-MOFs after hydrolysis reveals the binding of the phosphonic acid product to the MOF surface in monodentate and bidentate fashion, limiting turnover.[20,21] To circumvent bidentate coordination of phosphonate products to two adjacent Zr atoms on the MOF's SBU, a recent computational study by Mendonca and Snurr has probed the hydrolysis of sarin (GB, propan-2-yl methylphosphonofluoridate) on single transition-metal atoms supported by NU-1000.[22] In that landmark work, the Zr-MOF is functionalized with an impressive range of single transition-metal atoms, which are anchored to the SBU by bridging oxo or hydroxo ligands, depending on the oxidation state of the metal. Such single-atom modification elicits the possibility of nerve-agent hydrolysis on Lewis acid sites beyond those present in the native Zr-MOFs (Zr(IV)). In addition, functionalizing two adjacent Zr(IV) sites with a single atom mitigates irreversible bidentate binding of the product phosphonic acid to the MOF's SBU and advances the possibility of turnover at the gas−surface interface. In the explored reaction mechanism by Mendonca and Snurr, the single atom anchored to the MOF

Received: February 28, 2024
Revised: May 10, 2024
Accepted: May 17, 2024
Published: May 24, 2024

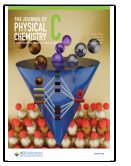

both serves as the binding site for sarin and features a terminal −OH ligand that acts as the base in the hydrolytic process. After water addition to the phosphorus center, a Berry pseudorotation step was required in the hydrolysis mechanism to produce a geometry that can lead to HF elimination and regeneration of the catalyst. The nature of the single atom influenced the rate-limiting step, which, in most cases, was either the Berry pseudorotation or the phosphonic acid product desorption. All examined single atoms exhibited lower product desorption energies than from the native Zr(IV) sites, highlighting the promise of single-atom functionalization of Zr-MOFs for nerve-agent hydrolysis.

Earlier computational work on the hydrolysis of sarin by UiO-66 showed a sensitivity of the stationary-point energies in the reaction mechanism to the conformational orientation of the nerve agent in the addition step.[23] In this work, we use high-level electronic structure methods to examine whether the conformational space available in the binding of sarin to a single transition-metal atom on MOF-808 influences the reaction mechanism. The results show a rich mechanistic diversity that includes novel hydrolysis mechanisms without a Berry pseudorotation step and the possibility of both HF and isopropanol elimination products. The use of high levels of electron correlation theory that transcend density-functional-theory techniques also allows us to benchmark the performance of popular DFT methods. Our work is performed on single atoms of Zn(II) and Ti(IV) anchored to MOF-808 (SA@MOF-808). As shown below, the way these single atoms are bound to the SBU depends on their oxidation state, so our choice of Zn(II) and Ti(IV) explores two anchoring motifs of the metals to the MOF (via bridging hydroxo and oxo ligands, respectively). In addition, the reported rate-limiting step for Zn(II) and Ti(IV) in NU-1000 is different:[22] product desorption is limiting for Zn(II), but the addition/elimination steps that take place earlier in the mechanism exhibit a higher barrier for Ti(IV). Our choice of Zn(II) and Ti(IV), therefore, allows us to probe the extent to which the possible rate-limiting steps apply to other MOF supports.

METHODS

All geometry optimizations were conducted with the B97D functional,[24] the def2-SVP basis set,[25] and an "ultrafine" integration grid as implemented in the Gaussian 09 program suite.[26] The calculations leveraged density fitting[27] and employed standard cutoffs. Harmonic frequency calculations and thermal Gibbs energy corrections were also obtained at the B97D/def2-SVP level. Energies were refined via single-point calculations in ORCA 5.0.4[28] using a variety of electronic structure methods and the def2-TZVP basis set.[25] The sensitivity of the reaction energy profile to the calculation method was explored with a variety of functionals including M06-L,[29] M06-2X,[30] B3LYP,[31] ωB97X,[32] and ωB97M[33] with D3BJ,[34] D3 (with zero damping),[35] and nonlocal[36] empirical-dispersion corrections. We transcended DFT by obtaining energies at the MP2 (using the resolution-of-the-identity approximation, RIMP2[37]), CCSD, and CCSD(T) (under the domain local pair natural orbital, DLPNO, approximation[38] with tight cutoffs) levels. Additional details of these highly accurate calculations are presented in Table S1. The energy profiles in this manuscript report RIMP2/def2-TZVP energies unless otherwise specified. All results correspond to the lowest-energy singlet state for the d^0 Ti(IV) and d^{10} Zn(II) systems. The lowest-energy triplet states appear more than 300 kJ/mol above the ground state for the catalyst structures, which justifies the exclusive consideration of singlet state throughout the reaction.

The previous single-atom work by Mendonca and Snurr employed the SBU of the NU-1000 Zr-MOF.[22] The SBU of MOF-808 used in this work retains the same SBU stoichiometry as NU-1000, but is 6- rather than 8-connected. Mendonca and Snurr verified that the description of aromatic linkers minimally affected the energy profile, as cluster models using benzoate or formate capping ligands provided similar energetics. Similar conclusions were obtained in earlier work with UiO-66 Zr-MOF.[23] The bulk of this work uses a cluster model of MOF-808 in which the 6 aromatic benzene-1,3,5-tricarboxylate linkers of the SBU are approximated by formate ligands. However, the main conclusions are validated using benzoate capping ligands in which the C atoms are held fixed to their crystallographic positions and with a model that considers two adjacent SBUs. Following earlier work on NU-1000,[39] a full coordination sphere of the Zr(IV) atoms in the MOF-808 SBU is achieved by the addition of alternating hydroxo and aqua ligands. As shown in Figure 1, the Zn(II) and Ti(IV) atoms are inserted as $[Zn(II)-OH_t]^+$ and $[Ti(IV)-OH_t]^{3+}$ moieties, where the $-OH_t$ group is a terminal hydroxo ligand that acts as the base during hydrolysis and is envisioned to originate from ambient water after removal of one proton. These moieties are inserted between a pair of hydroxo and aqua ligands on adjacent Zr(IV) atoms of the SBU. To maintain charge neutrality, an additional proton from the aqua ligand is removed for Zn(II) to yield two bridging hydroxo ligands. For Ti(IV), all three protons from the aqua and hydroxo ligands on the supporting Zr(IV) atoms are removed to yield a neutral catalyst anchored to the MOF via bridging oxo ligands.

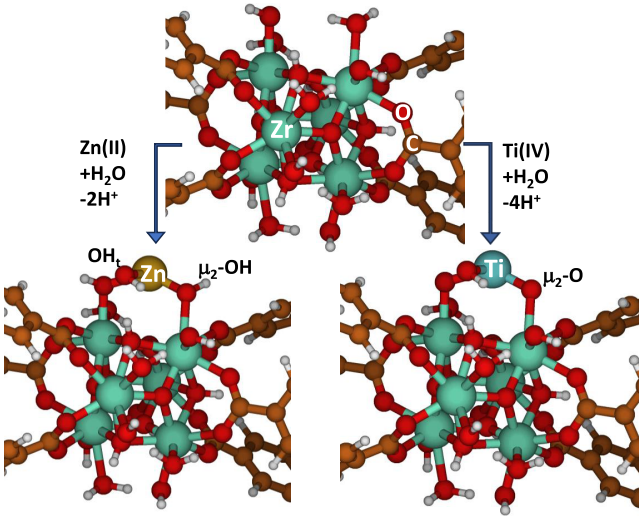

Figure 1. Schematic representation of the functionalization of MOF-808 (top) with Zn(II) or Ti(IV) single atoms (bottom). The Zn(II) and Ti(IV) single atoms are anchored to the SBU via bridging hydroxo or oxo ligands, respectively, and feature a terminal hydroxo ligand ($-OH_t$) that acts as the base in hydrolysis of organophosphorus nerve agents.

RESULTS

Reaction Mechanisms of GB Hydrolysis with Zn(II)@MOF-808. The first step in the hydrolysis reaction is the

https://doi.org/10.1021/acs.jpcc.4c01312
J. Phys. Chem. C 2024, 128, 8983−8992

binding of sarin to the single transition-metal atoms via the phosphoryl P═O group to form a coordination complex (Cat-GB). In this complex, rotation around the coordinate covalent bond formed between Zn and the sp^2 O atom of sarin allows for conformational isomerism (Figure 2). In addition,

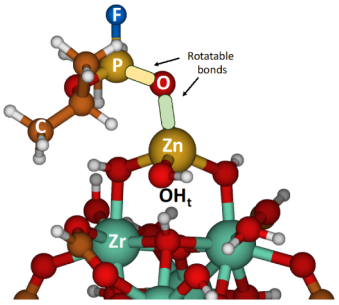

Figure 2. Schematic of the Cat-GB complex, highlighting the P−O (yellow) and Zn−O (green) rotatable bonds that lead to conformational isomerism. The various isomers reached by rotations around the highlighted bonds provide a diverse set of hydrolysis reaction mechanisms.

coordination to Zn(II) reduces the P═O group double-bond character, enabling low-barrier rotation around this bond in Cat-GB as well (P−O Mayer bond orders are 2.0 and 1.6, respectively, for sarin and Cat-GB at the B3LYP/def2-TZVP level).

To characterize the conformational space spanned by rotation around these two bonds, we have scanned the potential energy surface along the P−O−Zn−OH_t and iOPr−P−O−Zn dihedrals (Figures S1 and S2). From this conformational sampling, we have identified 9 Cat-GB conformers from which the hydrolysis reaction can proceed (Figure 3). In the figure, the isomers in a row are interconverted via rotation around the P−O bond and those in a column by rotation around the Zn−O bond. The isomers can be distinguished by the values of key dihedral angles. Thus, the top, middle, and bottom rows can be roughly classified as having large negative (<−80°), small (−37° — + 17°), or large positive (>+70°) P−O−Zn−OH_t dihedral angles, respectively. Within a row, rotation around the P−O bond acts to exchange the positions of the −F, −iOPr, and −CH_3 groups of sarin. These 9 isomers span an energy spectrum of 32 kJ/mol and are connected through low barriers (Figures S1 and S2). The central column of Figure 3 exhibits the three highest-energy conformers. In this isomer group, the −iOPr substituent is furthest from the MOF, and the decreased stability can, therefore, be attributed to the loss of intermolecular interactions with the SBU.

To deepen our understanding of the effect of conformational isomerism on reactivity, we have mapped hydrolysis reaction mechanisms starting from each conformer in Figure 3. From the Cat-GB complex, the steps of the reaction mechanism are (i) water binding to the Zn−OH_t base, (ii) concerted protonation of the Zn−OH_t base via water dissociation and nucleophilic addition of the nascent hydroxide to the P atom of sarin, (iii) formation of a pentacoordinated phosphorus intermediate (P5), (iv) elimination of −F or −iOPr from P5 to generate HF or iPrOH and the corresponding phosphonic acids, and (v) desorption of products to regenerate the catalyst. Our calculations show that the 9 possible pathways reduce to 6 at the addition transition state. The 3 conformers in the middle row of Figure 3 (small P−O−Zn−OH_t dihedrals) show

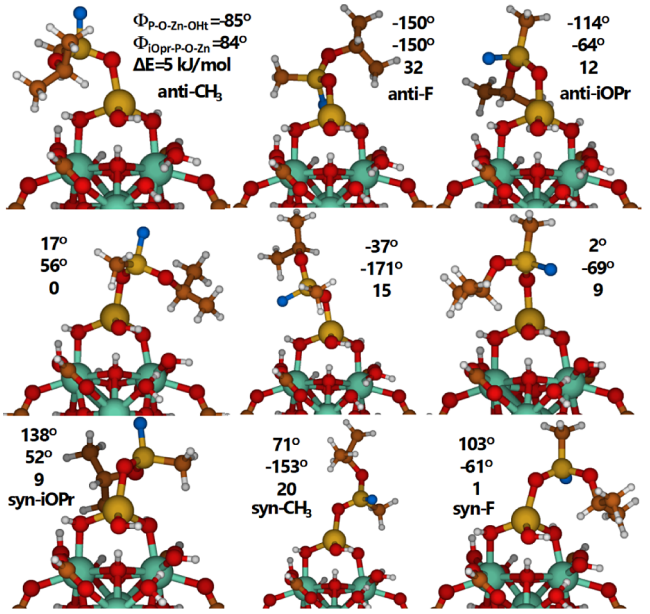

Figure 3. Schematic of the 9 Cat-GB complexes obtained via dihedral scans. The numbers are values of the P−O−Zn−OH_t dihedral angle (top, degrees), iOPr−P−O-Zn dihedral angle (middle, degrees), and relative energy (bottom, kJ/mol, RIMP2/def2-TZVP level). The conformers in the same row are interconverted via iOPr−P−O−Zn dihedral rotation and those in a column via P−O−Zn−OH_t rotation. The labels syn- and anti- refer to the orientation of the P═O bond with respect to the ZnO−H_t bond of the ZnOH_t base, and the labels −F, −CH_3, and −iOPr are for the group that is collinear with the OH nucleophile at the addition transition state. Data correspond to a formate-linker model. Results with benzoate ligands are in Figure S3.

various moieties of sarin encumbering the Zn−OH_t base. Water binding and subsequent deprotonation on the Zn−OH_t base can then only proceed with a rotation around the Zn−O bond that alleviates crowding of the base with the sarin groups. Such torsion transforms these 3 isomers into some of the other 6.

We distinguish the 6 remaining isomers using two structural features. First, we use the direction of the P═O bond with respect to the O−H bond of the Zn−OH_t base to separate two groups of three isomers. In "anti" isomers, the P═O bond points in a direction opposite to the ZnO−H_t bond (top row in Figure 3), and in the "syn" group of isomers, these two bonds point in the same direction (bottom). Within each syn or anti group, the isomers can be separated by the orientation of the −F, −CH_3, or −iOPr group (P═O bond rotation). Specifically, we label each of these isomers with the group whose bond to phosphorus is collinear with the incoming OH nucleophile at the addition transition state. Thus, in the anti-F isomer, the P═O bond points in a direction opposite to the ZnO−H_t bond, and the P−F bond is collinear with the forming P−OH bond at the addition transition state. In the following, we describe the reaction mechanisms for each of these 6 different conformers.

The catalytic cycle for the anti-CH_3 conformer of Zn(II)@MOF-808 is displayed in Figure 4 (ball-and-stick geometries in Figure S22). The reaction starts with water addition to Cat-GB to generate a reagents complex (R). From R, water protonates the Zn−OH_t base to generate a hydroxide nucleophile that adds concertedly to the P atom of sarin. The P−OH and P−CH_3 bonds are nearly collinear at the addition transition state

https://doi.org/10.1021/acs.jpcc.4c01312
J. Phys. Chem. C 2024, 128, 8983−8992

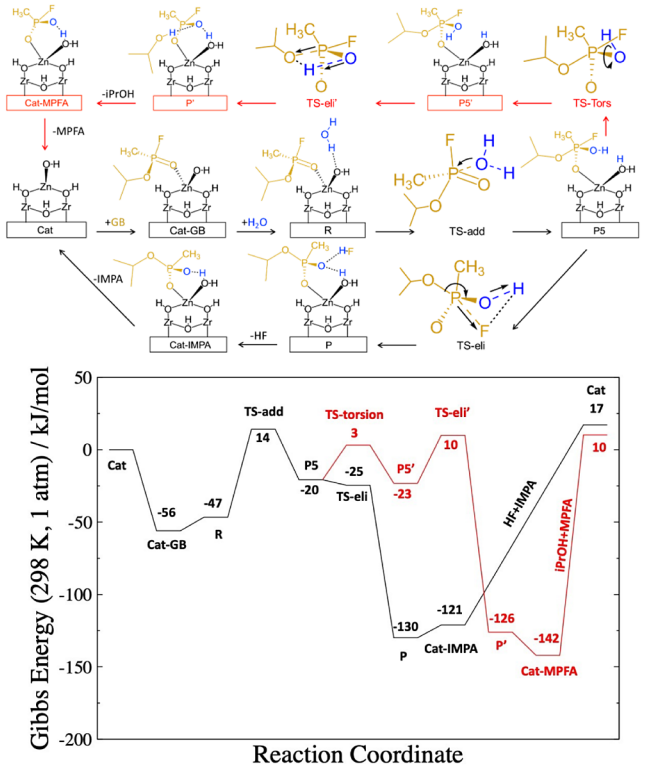

Figure 4. (Top) Reaction mechanism for hydrolysis of sarin by Zn(II)@MOF-808 along the anti-CH_3 pathway. The mechanism bifurcates into two branches, HF elimination (bottom panels) and iPrOH elimination (red, top panels). (Bottom) Gibbs energy profile (298 K, 1 atm) at the RIMP2/def2-TZVP level. Ball-and-stick geometries are shown in Figure S22.

(TS-add). A trigonal bipyramidal pentacoordinated phosphorus intermediate (P5) follows the addition transition state. As it has been previously discussed,[23] elimination of −F (or −iOPr) from the P5 intermediate requires an axial placement of the group in the trigonal bipyramid. In the P5 intermediate of Figure 4, the −F and −iOPr substituents are both in axial positions, so elimination can proceed directly without an intervening Berry pseudorotation step that reorganizes the intermediate. The HF elimination transition state (bottom branch in Figure 4) yields a products complex (P) in which HF is hydrogen bonded to the MOF and the isopropyl methylphosphonic acid (IMPA) coproduct is bound to the Zn center. The catalyst is regenerated upon desorption of both products.

Elimination of iPrOH can also proceed from P5 (top branch in Figure 4, red). First, the proton required for elimination of the −iOPr group is placed in the appropriate orientation via a torsion of the P−OH bond. The new P5′ intermediate that follows this torsion can reach the elimination transition state via lengthening of the P−iOPr bond to generate hydrogen-bonded iPrOH and methyl phosphonofluoridic acid (MPFA). The desorption of these products regenerates the catalyst. The energy profile in Figure 4 reveals that the elimination of iPrOH proceeds through a larger barrier than of HF. Products along both elimination channels are strongly bound to the catalyst, with desorption of the MPFA phosphonic acid being 14 kJ/mol more endoergic than of the IMPA product.

To calibrate the suitability of MOF-808 cluster models capped with formate ligands, we have calculated the lowest-energy pathway in Figure 4 with a MOF model featuring benzoate linkers in which the aromatic C atoms are frozen in their crystallographic positions. Figure S4 shows a somewhat uniform lowering of the relative energies of intermediate steps in the aromatic model by less than 10 kJ/mol for most steps compared to the reagent and product asymptotes. The increased dispersion interactions afforded by the aromatic moieties modulate the stationary-point energies but do not appear to affect the reaction energy profile dramatically.

We now review the mechanism and energy profiles of the other Cat-GB isomers to learn the role played by the starting isomer in the hydrolytic chemistry. Figure 5 exhibits the

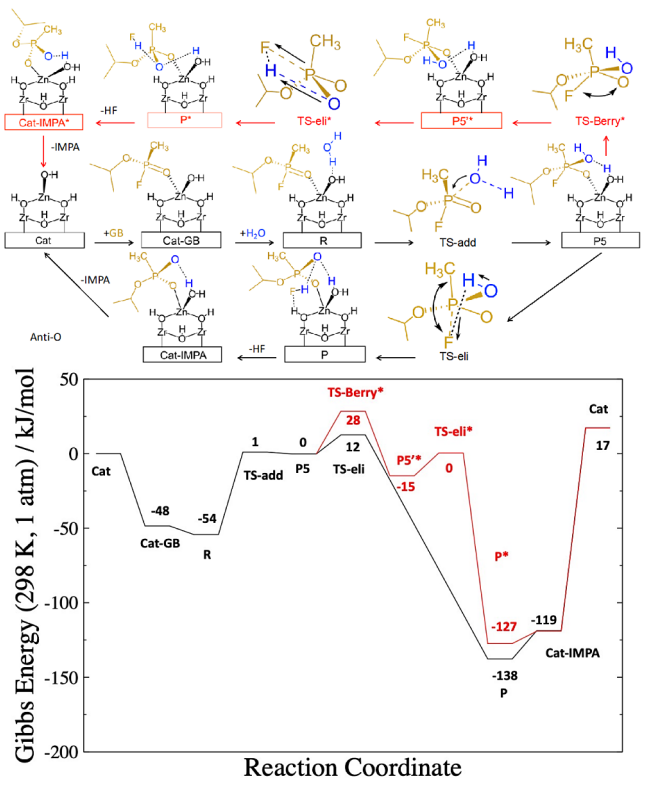

Figure 5. (Top) Reaction mechanism for hydrolysis of sarin by Zn(II)@MOF-808 along the anti-iOPr pathway. The mechanism bifurcates into two branches depending on the rearrangement of the P5 intermediate. Widening the F−P−CH_3 angle leads directly to HF elimination (bottom panels). Widening the F−P−O(Zn) angle also leads to HF elimination, through a more complex reaction mechanism (red, top panels). (Bottom) Gibbs energy profile (298 K, 1 atm) at the RIMP2/def2-TZVP level. Ball-and-stick geometries are shown in Figure S23.

mechanism and energy profile with the anti-iOPr isomer (ball-and-stick structures in Figure S23). The mechanism bifurcates into two paths at the P5 intermediate formed after nucleophilic addition. In this P5 intermediate, the −OH nucleophile and −iOPr group are in the axial sites of the trigonal bipyramid. The −F group is in an equatorial position, requiring a rearrangement of the trigonal bipyramid before elimination. We have examined two possible Berry pseudorotations to relocate the −F group from equatorial to axial placement. In the first pseudorotation, we widen the F−P−CH_3 angle in P5 from ∼120° to ∼180° (bottom branch in Figure 5). The pseudorotation transition state along this branch leads directly to HF elimination without an intervening P5 intermediate. In

https://doi.org/10.1021/acs.jpcc.4c01312
J. Phys. Chem. C 2024, 128, 8983−8992

the second pseudorotation, we widen the F−P−O(Zn) angle (top branch, red). The transition state for this rearrangement is 16 kJ/mol higher in energy and yields a stable P5′ intermediate with −F and −O(Zn) substituents in axial positions. Elimination proceeds via concerted dissociation and formation of the P−F and F−H(O) bonds, respectively.

The anti-F conformer is the last of the anti series. However, this conformer isomerizes to syn-F at the addition transition state, so we now describe the syn series. Figure 6 shows the

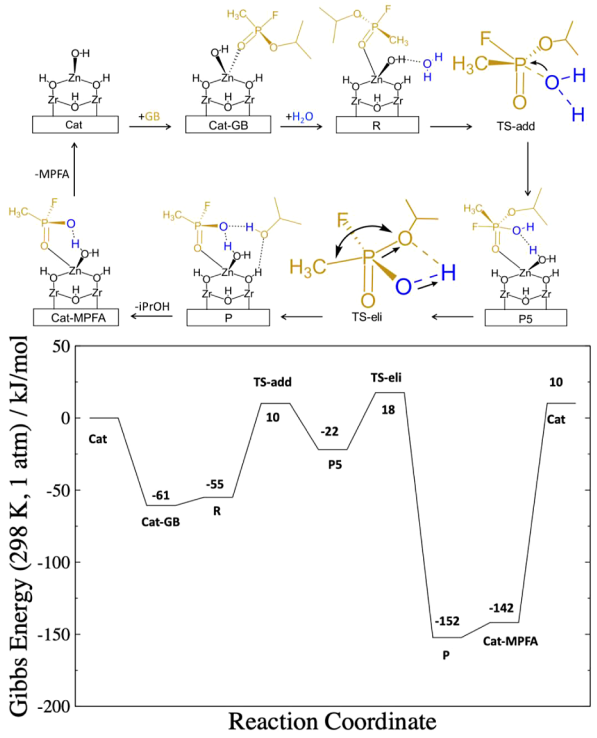

Figure 6. (Top) Reaction mechanism for hydrolysis of sarin by Zn(II)@MOF-808 along the syn-F pathway. (Bottom) Gibbs energy profile (298 K, 1 atm) at the RIMP2/def2-TZVP level. Ball-and-stick geometries are shown in Figure S24.

syn-F mechanism and energy profile. With the syn-F conformer, the −F and −OH groups are both in axial at the P5 stage. This complicates HF elimination, as the −OH group needs to be in an equatorial position to transfer a proton to the eliminating −F group. However, iPrOH elimination can proceed directly from P5 by widening the CH_3−P−iOPr angle without the formation of a subsequent P5 intermediate. The energy profile in Figure 6 demonstrates that the barrier for iPrOH elimination is competitive with some of the HF elimination channels reported so far in Figures 4 and 5. This alcohol elimination channel has so far been overlooked in the sarin hydrolysis literature, where most efforts have been directed at characterizing HF elimination.[8] However, the study of this channel here is instructive because in work with nerve-agent mimics such as methyl-paraoxon, alcohol elimination is the only possible pathway.[12]

Much as with the convergence of anti- and syn-F pathways, our calculations of the syn-CH_3 pathway shifted to the anti-CH_3 mechanism in Figure 4 at the addition transition state. The last of the 6 hydrolysis pathways is, therefore, syn-iOPr, shown in Figure S5. This mechanism is analogous to the one in Figure 5 for the anti-iOPr pathway: after a P5 intermediate with −OH and −iOPr in axial positions, widening of the CH_3−P−F angle proceeds through a lower barrier than the pseudorotation that places the −F and −O(Zn) groups in axial. While the P5′ intermediates ensuing both pseudorotations are comparably stable, elimination from the P5′ intermediate where the $-CH_3$ group is coaxial with −F is markedly less costly than when the −O(Zn) group is coaxial with −F.

An energy-profile comparison of the wide variety of mechanisms described so far for sarin hydrolysis by Zn(II)@MOF-808 is displayed in Figure 7, and numerical values of all

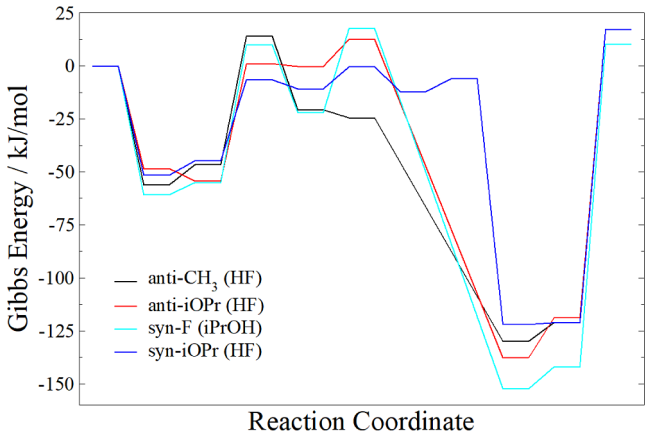

Figure 7. Comparison of energy profiles along the lowest-energy branches of all symmetry-inequivalent pathways in the hydrolysis of sarin by Zn(II)@MOF-808. Data correspond to Gibbs energies at the RIMP2/def2-TZVP level. Transition-state energies are provided in Table S2.

barriers are collected in Table S2 (a complementary set of energy profiles at the B3LYP-D3BJ/def2-TZVP level is given in Figures S10−S13). Only the lowest-energy branch of each isomeric pathway is shown in the figure for clarity. The compared profiles in Figure 7 reveal that while for most pathways the highest barrier prior to desorption is in either the pseudorotation or elimination steps, the addition step is more energetic than pseudorotation or elimination for the anti-CH_3 pathway. This can be rationalized considering the composition of the sarin's tetrahedral face that the hydroxide nucleophile encounters during its addition to the phosphorus center (Figure S25). In anti-CH_3, the tetrahedral face of sarin that hydroxide approaches during addition is formed by all the electron-rich atoms coordinated to the phosphorus center (−F, −iOPr, and =O), which enhances repulsion. In the rest of the pathways, the methyl moiety replaces −F or −iOPr in the tetrahedral face proximal to the incoming hydroxide, resulting in lower addition barriers compared to anti-CH_3. Importantly, based on energetic-span-model considerations,[40] product desorption is rate-limiting for all pathways, as it requires more than 60 kJ/mol more energy than the preceding addition/elimination barriers.

Reaction Mechanisms of GB Hydrolysis with Ti(IV)@MOF-808. We now turn our attention to examining whether the diversity of reaction mechanisms described for hydrolysis with Zn(II) extends to other metals. We choose Ti(IV) for this comparison because the catalyst structure is significantly different from that of Zn(II). As shown in Figure 1, installation of a + 4 ion with a terminal −OH ligand in MOF-808 results in the anchoring of a Ti(IV)—OH moiety to the MOF via

https://doi.org/10.1021/acs.jpcc.4c01312
J. Phys. Chem. C 2024, 128, 8983−8992

bridging oxo ligands. In the Zn(II) catalyst, the single atom is anchored via two bridging hydroxo ligands instead (Figure 1). As we show below, the difference between bridging hydroxo and oxo ligands influences the reaction mechanism.

The anti-CH_3 pathway on Ti(IV)@MOF-808 is shown in Figure S6. The early steps of the reaction mechanism are reminiscent of the reaction with Zn(II) (Figure 4), including the fact that the addition step exhibits a higher barrier than elimination and that a Berry pseudorotation is not necessary before the elimination of HF. A difference between Zn(II) and Ti(IV) is that the HF product is not formed directly in the Ti(IV) catalyst. Instead, following the elimination transition state, the F moiety forms a coordinate covalent bond with the Ti(IV) Lewis acid. The product complex, therefore, exhibits a Ti−F bond and is lower in energy than the counterpart HF product obtained with Zn(II) (59 kJ/mol HF desorption Gibbs energy in Ti(IV) vs 9 kJ/mol in Zn(II)). Given that the Zn(II) calculations show that iPrOH formation from P5 with this conformer requires a significantly larger barrier than HF and that the elimination barrier of HF is only 3 kJ/mol above the P5 intermediate for Ti(IV), we have not mapped the iPrOH elimination pathway with Ti(IV).

Figure S7 displays the anti-iOPr pathway. As with Zn(II), the trigonal bipyramidal P5 intermediate can rearrange to place the −F substituent in axial in two different ways, by opening either the F−P−CH_3 or F−P−O(Ti) angle, so that the −CH_3 or −O(Ti) groups are located coaxially to −F, respectively. The pseudorotation that produces a linear F−P−CH_3 arrangement proceeds with a barrier 14 kJ/mol lower, following the trend discussed before for Zn(II). However, in contrast with Zn(II), this pseudorotation does not lead directly to HF elimination. Instead, a very shallow P5′ intermediate is obtained, which proceeds to products through a small barrier. Similarly to the anti-CH_3 pathway, elimination results in a Ti−F bond that considerably deepens the potential energy well of the P complex. Interestingly, the higher-energy pseudorotation places the −F moiety far apart from the Ti center (upper branch in the top panel of Figure S7), leading to the formation of gas-phase HF instead of a Ti−F bond.

As with Zn(II), the anti-F pathway converges in the addition transition state to the syn-F pathway, shown in Figure S8. (The syn-CH_3 pathway similarly converts to the anti-CH_3 mechanism discussed in Figure S6.) In the P5 intermediate of the syn-F mechanism, −F is coaxial with −OH, so the most direct elimination route is a pseudorotation of the equatorial −iOPr group, which leads to iPrOH elimination without an intervening P5 intermediate. Remarkably, the iPrOH product is not weakly adsorbed to the MOF via hydrogen bonds. Instead, the alcohol binds to Ti(IV), much as has been described at titania surfaces with open Ti(IV) sites.[41] This convergence of bonding patterns suggests that the voluminous work on the chemistry of nerve agents with extended metal-oxide surfaces[42−45] can inform studies on the discrete metal-oxide cores of MOFs. The P complex featuring an alcohol coordination to the Ti(IV) Lewis acid is notably deeper (44 kJ/mol iPrOH Gibbs desorption energy in Ti(IV)) than the hydrogen-bonded complex described for Zn(II) in the same channel (10 kJ/mol, Figure 6).

The last hydrolysis channel on Ti(IV) is syn-iOPr (Figure S9). Here, the mechanistic variants follow those described in Zn(II): the Berry pseudorotation needed to place the −F group in axial is 11 kJ/mol more energetic when the resulting coaxial group is −O(Ti) than when it is −CH_3. In addition, the lower-barrier branch generates a deep P complex with a Ti−F bond, but gas-phase HF is generated in the higher-energy pathway.

Figure 8 compares the lowest-energy isomeric pathways for sarin hydrolysis with Ti(IV) at the RIMP2/def2-TZVP level

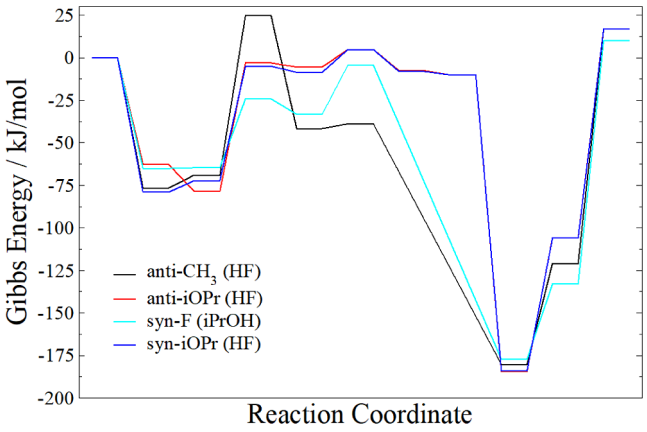

Figure 8. Comparison of energy profile along the lowest-energy branches of the 6 conformational pathways in the hydrolysis of sarin by Ti(IV)@MOF. Data correspond to Gibbs energies at the RIMP2/def2-TZVP level. Transition-state energies are provided in Table S2.

(transition-state energies in Table S2, and B3LYP-D3BJ/def2-TZVP energy profiles in Figures S14−S17). Noticeably, the overall lowest-energy path in the addition−elimination steps produces iPrOH instead of HF products. Nevertheless, desorption of the phosphonic acid products (143 kJ/mol from Cat-MPFA and 138 kJ/mol from the deepest Cat-IMPA complex) is more than 50 kJ/mol more endoergic than the lowest-energy barrier of all preceding steps, making product desorption rate-limiting overall.

To evaluate the differences in the hydrolytic chemistry of Zn(II) and Ti(IV) centers, Figure 9 compares the anti-CH_3 pathways for both metals obtained with benzoate capping ligands (geometries available in Figures S18 and S19). For both metals, addition is significantly more energetic than

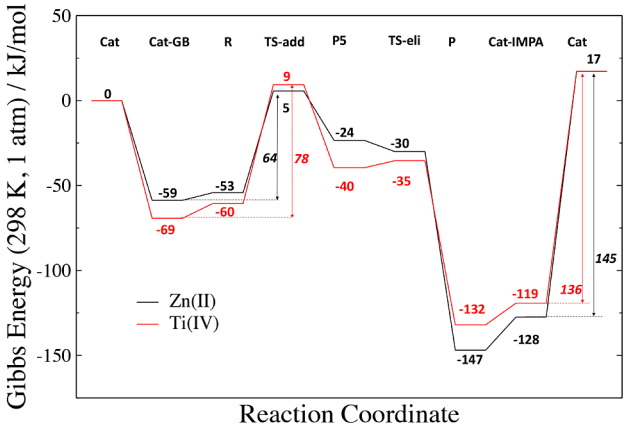

Figure 9. Gibbs energies (298 K, 1 atm) for the anti-CH_3 pathway in the hydrolysis of sarin with Zn(II) and Ti(IV)@MOF-808. Numbers in plain font represent energies relative to separated reagents in kJ/mol. The figure highlights (italicized numbers) the comparison of IMPA desorption energies with the highest preceding barrier (addition, determined from the Cat-GB minimum). RIMP2/def2-TZVP values obtained with the benzoate-ligand model.

https://doi.org/10.1021/acs.jpcc.4c01312
J. Phys. Chem. C 2024, 128, 8983−8992

elimination. Further, product desorption is more than 50 kJ/mol more energetic than the highest barrier in the preceding steps (addition) with both Zn(II) and Ti(IV). While product desorption is rate-limiting for the single-atom MOFs in this work, there is a marked reduction in the desorption energy compared to that in the native MOF-808 of 32 and 41 kJ/mol for Zn(II) and Ti(IV)@MOF-808, respectively (Figure S20). This is important because product inhibition of the catalyst has been experimentally verified in various Zr-MOFs.[20,21] The reduction in product binding energy with single-atom functionalization of MOFs, therefore, advances the quest toward catalytic hydrolysis of nerve agents at the gas−surface interface.

We have aimed to further validate the conclusion that product desorption is rate-limiting drawn from our cluster models by examining the effect of a proximal SBU on the energy of the desorption step. Figure S21 depicts the geometry of IMPA in the large pore of Zn(II)@MOF-808 together with the benzoate-linker model used in Figure 9 and the two-SBU model. Use of benzoate capping ligands appears to be reasonably accurate, as the presence of the neighboring SBU stabilizes the product by only an additional 5 kJ/mol, or 3% of the desorption energy.

High-Accuracy Benchmarks. Computational studies of catalytic processes in MOFs have long helped accelerate the understanding of these systems.[46] Due to the high-polynomial scaling of accurate electronic-structure methods with system size, typical calculations are restricted to efficient DFT techniques. However, the performance of DFT for specific catalysts remains in question due to the lack of high-accuracy benchmarks. The unabated interest in CWA decomposition on MOFs provides motivation to perform such high-accuracy benchmarks in this work that calibrate the performance of DFT techniques.

While second-order Møller−Plesset calculations like those shown in the energy diagrams of Figures 4−9 are commonly considered to be a step up from standard DFT methods, their accuracy for catalytic systems involving transition metals in MOFs has not been thoroughly determined. We, therefore, have involved the "gold standard" of single-reference electronic structure calculations, CCSD(T), in an attempt to provide an authoritative benchmark for both MP2 and DFT methods. Even with the use of the DLPNO approximation,[38] the tremendous computational overhead of CCSD(T) calculations when using the def2-TZVP basis set has limited our benchmark work to reaction energies for both HF + IMPA and iPrOH + MPFA channels, the deepest Cat-GB and Cat-IMPA complexes with both Zn(II) and Ti(IV) systems, the lowest-energy Berry pseudorotation transition state for the syn-iOPr pathway with Zn(II), and the R, TS-add, and lowest-energy TS-eli stationary points in anti-iOPr with Ti(IV)—a total of 10 points.

Figure 10 shows the mean and maximum unsigned deviations between the predictions of a variety of methods and the DLPNO−CCSD(T) calculations, all with the def2-TZVP basis set. DLPNO−CCSD and RIMP2 energies, respectively, underestimate and overestimate the CCSD(T) benchmark energies somewhat consistently to produce mean deviations of 8−9 kJ/mol. Maximum deviations are 16−17 kJ/mol. Turning to computationally intensive double hybrid DFT methods, B2PLYP does not appear appropriate for the chemistry in this work. PWPB95 performs better than RIMP2 and CCSD, but only with D3BJ dispersion. This result highlights the importance of empirical dispersion in DFT techniques, even when correlation corrections at the MP2 level are employed, as in double-hybrid functionals. The range-separated ωB97X functional performs superbly in combination with either D3BJ or nonlocal dispersion (ωB97X-V). The mean deviation from CCSD(T) is impressively under 4 kJ/mol, and the maximum deviation is below 10 kJ/mol. The ωB97M variant is only slightly less accurate.

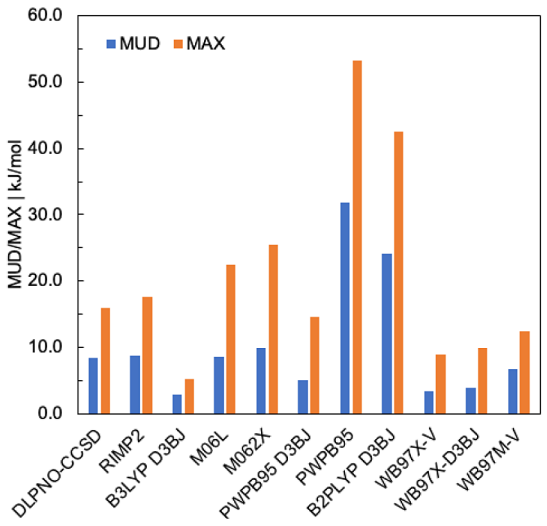

Figure 10. Mean unsigned deviation (MUD) and absolute maximum deviations (MAX) of various electronic structure methods compared to the DLPNO−CCSD(T)/def2-TZVP benchmarks for 10 stationary-point energies in the hydrolysis of sarin with Ti(IV) and Zn(II)@MOF-808 catalysts.

M06-L has arguably been the most popular functional for nerve-agent work with MOFs,[22,47−50] as its pure, meta-GGA nature makes it very efficient in combination with density fitting. Here, we see mean deviations with respect to CCSD(T) of 9 kJ/mol. However, the maximum deviation is large (22 kJ/mol). M06-2X does not improve over M06-L, exhibiting a maximum deviation of over 25 kJ/mol. B3LYP, in combination with D3BJ dispersion, exhibits shocking accuracy considering its low cost (3 (5) kJ/mol mean (maximum) deviation), and it outperforms the rest of the techniques discussed here, even those beyond DFT. The maximum deviation for B3LYP-D3BJ occurs for the HF + IMPA reaction energy and not for any points involving the transition-metal catalyst. If this level of accuracy was maintained for other metals, B3LYP-D3BJ would emerge as the most attractive technique for the study of nerve-agent hydrolysis on transition-metal catalysts like those sampled here. In the absence of additional benchmarks, the higher methodological robustness of the range-separated ωB97X-V functional would lend more confidence to its use, despite the increased computational expense.

DISCUSSION

A detailed exploration of the conformational energy landscape in the hydrolysis of sarin by single transition-metal atoms on MOF-808 reveals a diversity of reaction pathways, which vary in the product formed (HF + IMPA vs iPrOH + MPFA), the generation of these products via rearrangement of intermediates, and their energetic demands. In prior work by Mendonca and Snurr,[22] variations across 36 transition-metal/oxidation state combinations were performed to understand the role of the metal on the reaction energy profile. Such a tremendous

https://doi.org/10.1021/acs.jpcc.4c01312
J. Phys. Chem. C 2024, 128, 8983−8992

undertaking was performed for just one of the reaction channels described in this manuscript, which we have labeled as syn-iOPr. The authors explored the syn-CH_3 and syn-F pathways as well for Ti(IV) and for convenience used only the −iOPr channel for the rest of the transition metals after noting an insensitivity of the energy profile to the substituent in axial position at the addition transition state. No anti channels or iPrOH elimination pathways were characterized, so the calculations reported here nicely complement the prior work with NU-1000.

More importantly, within the syn-iOPr conformer, Mendonca and Snurr mapped the pseudorotation pathway that locates the −F and −O(Zn) groups in axial sites before HF elimination. The calculations of this work reveal that a different pseudorotation placing the −F and $-CH_3$ groups in axial positions instead is of lower energy. For Zn(II), the differences in these two Berry pseudorotation transition states are 16 and 17 kJ/mol for anti-iOPr and syn-iOPr, while for Ti(IV), they are 14 and 11 kJ/mol, respectively.

Using NU-1000 as a MOF supporting the transition metal and M06-L calculations with a def2-TZVP basis set for the reactive atoms, Mendonca and Snurr concluded that for Ti(IV), the barrier for the addition/elimination steps (132 kJ/mol) was higher than the desorption energy of IMPA (112 kJ/mol) and, therefore, rate-limiting. In this work, we see that product desorption, rather than the preceding addition/elimination steps, is rate-limiting for both Ti(IV) and Zn(II)@MOF-808. Indeed, Figure 9 shows that for both Zn(II) and Ti(IV), the product desorption energies (145 and 136 kJ/mol, respectively) are greater than the highest barrier in the earlier steps (addition, 64 and 78 kJ/mol determined from the deepest preceding minima).

There are several reasons for the discrepancy with prior work in the rate-limiting step for Ti(IV). First, as mentioned before, limited sampling of conformational pathways might have not identified the lowest-energy pathway in the steps prior to desorption or the deepest Cat-IMPA product state, which would artificially increase the apparent addition/elimination barrier and decrease the desorption barrier. Additionally, the M06-L method used in prior work underestimates the DLPNO−CCSD(T) Cat-IMPA desorption energy by over 22 kJ/mol. These factors contribute to updating the rate-limiting step from addition/elimination to product desorption in sarin hydrolysis with Ti(IV) single atoms at Zr-MOFs in this work. Two caveats in this comparison with prior work should be noted. Fist, the supporting Zr-MOFs cluster models are different (8-coordinated NU-1000 vs 6-coordinated MOF-808). Second, the previous calculations used the R enantiomer of sarin instead of the more toxic S enantiomer,[51] but this is unlikely to significantly impact the overall prediction stemming from this work.

CONCLUSIONS

This work evinces the importance of conformational isomerism in hydrolysis reactions of fluxional molecules such as nerve agents. Conformational sampling of the complex formed upon binding of the nerve agent sarin to single-atom@Zr-MOF catalysts reveals 6 possible hydrolysis pathways, which differ in the orientation of sarin with respect to the single-atom OH_t base. Detailed mapping of the hydrolysis mechanisms stemming from the 6 conformers reveals that in addition to the heavily studied HF elimination, iPrOH production proceeds through comparable barriers. Moreover, examination of various possible pseudorotations in a key pentacoordinated phosphorus intermediate leads to a new reaction path for the formation of HF that requires lower barriers than previously reported. A wealth of mechanistic possibilities is revealed, including the formation of products directly from addition−elimination steps without an intervening Berry pseudorotation, pathways in which either addition or elimination is rate-limiting before product desorption, and the formation of stable bonds between the −F group and the catalytic single atom.

An important aspect of this work is that gold-standard coupled-cluster calculations are used to lend confidence to the validity of the predictions. From these benchmarks, we conclude that the phosphonic acid product desorption from the catalyst is rate-limiting for both Zn(II) and Ti(IV) single atoms. Ameliorating product desorption will, therefore, be a key focus in the design of future catalysts that can efficiently hydrolyze nerve agents in the gas phase. The benchmark calculations also allow us to calibrate the accuracy of more efficient DFT methods for the transition-metal chemistry of this work. Both B3LYP-D3BJ and ωB97X-V perform remarkably well, improving over ab initio methods such as MP2 and CCSD. The assessment of DFT methods based on high-level calculations like the ones in this work will continue to be paramount in future computational work of catalytic processes involving transition metals.

ASSOCIATED CONTENT

Supporting Information

The Supporting Information is available free of charge at https://pubs.acs.org/doi/10.1021/acs.jpcc.4c01312.

Details of the def2-TZVP calculations, numerical values of barriers and imaginary frequencies, conformational scans for Cat-GB, complementary energy profiles for the hydrolysis of sarin with various models and calculation methods, ball-and-stick geometries of stationary points, product desorption energies in comparison with the native MOF-808, schematic of IMPA bound to Zn(II)@MOF-808 in the MOF's large pore, and tetrahedral faces of sarin encountered by the OH nucleophile during addition (PDF)

Geometries of Zn(II)@MOF-808 and Ti(IV)@MOF-808 stationary points (ZIP)

AUTHOR INFORMATION

Corresponding Author

Diego Troya − *Department of Chemistry, Virginia Tech, Blacksburg, Virginia 24060, United States;* orcid.org/0000-0003-4971-4998; Email: troya@vt.edu

Author

Carl Fossum − *Department of Chemistry, Virginia Tech, Blacksburg, Virginia 24060, United States;* orcid.org/0009-0003-7348-3568

Complete contact information is available at: https://pubs.acs.org/10.1021/acs.jpcc.4c01312

Author Contributions

All authors contributed to the development of this manuscript.

Notes

The authors declare no competing financial interest.

https://doi.org/10.1021/acs.jpcc.4c01312
J. Phys. Chem. C 2024, 128, 8983−8992

■ ACKNOWLEDGMENTS

This work was supported by the U.S. Army Research Laboratory and the U.S. Army Research Office under grant no. W911NF-20-2-0058. The views and conclusions herein are those of the authors and should not be interpreted as necessarily representing the official policies or endorsements, either expressed or implied, of the ARO or the U.S. Government. The authors acknowledge Advanced Research Computing at Virginia Tech for providing computational resources and technical support that have contributed to the results reported within this paper. URL: https://arc.vt.edu/.

■ REFERENCES

(1) Szinicz, L. History of chemical and biological warfare agents. *Toxicology* **2005**, *214* (3), 167−181.
(2) Compton, J. A. F. *Military chemical and biological agents: chemical and toxicological properties*; Telford Press, 1987.
(3) Tuorinsky, S. Medical Aspects of Chemical Warfare. In *Office of the Surgeon General*, Tuorinsky, S. D., Ed; TMM Publications: Washington, DC, 2008.
(4) Nikitin, M. B. D.; Jabbari, C. A. *Resurgence of Chemical Weapons Use: Issues for Congress*; CRS Reports , 2018.
(5) Enserink, M. U. N. Taps Special Labs to Investigate Syrian Attack. *Science* **2013**, *341* (6150), 1050−1051.
(6) Black, R. M.; Clarke, R. J.; Read, R. W.; Reid, M. T. J. Application of gas chromatography-mass spectrometry and gas chromatography-tandem mass spectrometry to the analysis of chemical warfare samples, found to contain residues of the nerve agent sarin, sulphur mustard and their degradation products. *J. Chromatogr. A.* **1994**, *662* (2), 301−321.
(7) Noort, D.; Hulst, A. G.; Platenburg, D. H. J. M.; Polhuijs, M.; Benschop, H. P. Quantitative analysis of O-isopropyl methylphosphonic acid in serum samples of Japanese citizens allegedly exposed to sarin: estimation of internal dosage. *Arch. Toxicol.* **1998**, *72* (10), 671−675.
(8) DeCoste, J. B.; Peterson, G. W. Metal−Organic Frameworks for Air Purification of Toxic Chemicals. *Chem. Rev.* **2014**, *114* (11), 5695−5727.
(9) Decoste, J. B.; Peterson, G. W.; Jasuja, H.; Glover, T. G.; Huang, Y.-G.; Walton, K. S. Stability and degradation mechanisms of metal−organic frameworks containing the Zr6O4(OH)4 secondary building unit. *J. Mater. Chem. A.* **2013**, *1* (18), 5642.
(10) Mondloch, J. E.; Katz, M. J.; Isley Iii, W. C.; Ghosh, P.; Liao, P.; Bury, W.; Wagner, G. W.; Hall, M. G.; DeCoste, J. B.; Peterson, G. W.; Snurr, R. Q.; et al. Destruction of chemical warfare agents using metal−organic frameworks. *Nat. Mater.* **2015**, *14* (5), 512−516.
(11) Katz, M. J.; Mondloch, J. E.; Totten, R. K.; Park, J. K.; Nguyen, S. T.; Farha, O. K.; Hupp, J. T. Simple and Compelling Biomimetic Metal-Organic Framework Catalyst for the Degradation of Nerve Agent Simulants. *Angew. Chem.* **2014**, *126* (2), 507−511.
(12) Moon, S.-Y.; Liu, Y.; Hupp, J. T.; Farha, O. K. Instantaneous Hydrolysis of Nerve-Agent Simulants with a Six-Connected Zirconium-Based Metal−Organic Framework. *Angew. Chem., Int. Ed.* **2015**, *54* (23), 6795−6799.
(13) Grissom, T. G.; Plonka, A. M.; Sharp, C. H.; Ebrahim, A. M.; Tian, Y.; Collins-Wildman, D. L.; Kaledin, A. L.; Siegal, H. J.; Troya, D.; Hill, C. L.; et al. Metal−Organic Framework- and Polyoxometalate-Based Sorbents for the Uptake and Destruction of Chemical Warfare Agents. *ACS Appl. Mater. Interfaces* **2020**, *12* (13), 14641−14661.
(14) Kirlikovali, K. O.; Chen, Z.; Islamoglu, T.; Hupp, J. T.; Farha, O. K. Zirconium-Based Metal−Organic Frameworks for the Catalytic Hydrolysis of Organophosphorus Nerve Agents. *ACS Appl. Mater. Interfaces* **2020**, *12* (13), 14702−14720.
(15) Cavka, J. H.; Jakobsen, S.; Olsbye, U.; Guillou, N.; Lamberti, C.; Bordiga, S.; Lillerud, K. P. A New Zirconium Inorganic Building Brick Forming Metal Organic Frameworks with Exceptional Stability. *J. Am. Chem. Soc.* **2008**, *130* (42), 13850−13851.
(16) Mondloch, J. E.; Bury, W.; Fairen-Jimenez, D.; Kwon, S.; DeMarco, E. J.; Weston, M. H.; Sarjeant, A. A.; Nguyen, S. T.; Stair, P. C.; Snurr, R. Q.; Farha, O. K. Vapor-Phase Metalation by Atomic Layer Deposition in a Metal−Organic Framework. *J. Am. Chem. Soc.* **2013**, *135* (28), 10294−10297.
(17) Furukawa, H.; Gándara, F.; Zhang, Y.-B.; Jiang, J.; Queen, W. L.; Hudson, M. R.; Yaghi, O. M. Water adsorption in porous metal−organic frameworks and related materials. *J. Am. Chem. Soc.* **2014**, *136* (11), 4369−4381.
(18) López-Maya, E.; Montoro, C.; Rodríguez-Albelo, L. M.; Lozano-Pérez, A. A.; Cenís, J. L.; Barea, E.; Navarro, J. A. R. Textile/Metal−Organic-Framework Composites as Self-Detoxifying Filters for Chemical-Warfare Agents. *Angew. Chem., Int. Ed.* **2015**, *54* (23), 6790−6794.
(19) Plonka, A. M.; Wang, Q.; Gordon, W. O.; Balboa, A.; Troya, D.; Guo, W.; Sharp, C. H.; Senanayake, S. D.; Morris, J. R.; Hill, C. L. In situ probes of capture and decomposition of chemical warfare agent simulants by Zr-based metal organic frameworks. *J. Am. Chem. Soc.* **2017**, *139* (2), 599−602.
(20) Terban, M. W.; Ghose, S. K.; Plonka, A. M.; Troya, D.; Juhás, P.; Dinnebier, R. E.; Mahle, J. J.; Gordon, W. O.; Frenkel, A. I. Atomic resolution tracking of nerve-agent simulant decomposition and host metal−organic framework response in real space. *Commun. Chem.* **2021**, *4* (1), 2.
(21) Wang, G.; Sharp, C.; Plonka, A. M.; Wang, Q.; Frenkel, A. I.; Guo, W.; Hill, C.; Smith, C.; Kollar, J.; Troya, D.; et al. Mechanism and Kinetics for Reaction of the Chemical Warfare Agent Simulant, DMMP(g), with Zirconium(IV) MOFs: An Ultrahigh-Vacuum and DFT Study. *J. Phys. Chem. C* **2017**, *121* (21), 11261−11272.
(22) Mendonca, M. L.; Snurr, R. Q. Computational Screening of Metal−Organic Framework-Supported Single-Atom Transition-Metal Catalysts for the Gas-Phase Hydrolysis of Nerve Agents. *ACS Catal.* **2020**, *10* (2), 1310−1323.
(23) Troya, D. Reaction Mechanism of Nerve-Agent Decomposition with Zr-Based Metal Organic Frameworks. *J. Phys. Chem. C* **2016**, *120* (51), 29312−29323.
(24) Grimme, S. Semiempirical GGA-type density functional constructed with a long-range dispersion correction. *J. Comput. Chem.* **2006**, *27* (15), 1787−1799.
(25) Weigend, F.; Ahlrichs, R. Balanced basis sets of split valence, triple zeta valence and quadruple zeta valence quality for H to Rn: Design and assessment of accuracy. *Phys. Chem. Chem. Phys.* **2005**, *7* (18), 3297−3305.
(26) Frisch, M. J.; Trucks, G. W.; Schlegel, H. B.; Scuseria, G. E.; Robb, M.A.; Cheeseman, J. R.; Scalmani, G.; Barone, V.; Mennucci, B.; Petersson, G. A. *Gaussian 09 Rev. E0.1*; Gaussian Inc: Wallingford, CT, 2009.
(27) Weigend, F. Accurate Coulomb-fitting basis sets for H to Rn. *Phys. Chem. Chem. Phys.* **2006**, *8* (9), 1057−1065.
(28) Neese, F.; Wennmohs, F.; Becker, U.; Riplinger, C. The ORCA quantum chemistry program package. *J. Chem. Phys.* **2020**, *152*, 22.
(29) Zhao, Y.; Truhlar, D. G. A new local density functional for main-group thermochemistry, transition metal bonding, thermochemical kinetics, and noncovalent interactions. *J. Chem. Phys.* **2006**, *125*, 19.
(30) Zhao, Y.; Truhlar, D. G. The M06 suite of density functionals for main group thermochemistry, thermochemical kinetics, noncovalent interactions, excited states, and transition elements: two new functionals and systematic testing of four M06-class functionals and 12 other functionals. *Theor. Chem. Acc.* **2008**, *120* (1), 215−241.
(31) Becke, A. D. Density-functional thermochemistry. I. The effect of the exchange-only gradient correction. *J. Chem. Phys.* **1992**, *96* (3), 2155−2160.
(32) Chai, J.-D.; Head-Gordon, M. Long-range corrected hybrid density functionals with damped atom−atom dispersion corrections. *Phys. Chem. Chem. Phys.* **2008**, *10* (44), 6615−6620.

https://doi.org/10.1021/acs.jpcc.4c01312
J. Phys. Chem. C 2024, 128, 8983−8992

(33) Mardirossian, N.; Head-Gordon, M. ωB97M-V: A combinatorially optimized, range-separated hybrid, meta-GGA density functional with VV10 nonlocal correlation. *J. Chem. Phys.* **2016**, *144*, 21.
(34) Najibi, A.; Goerigk, L. The Nonlocal Kernel in van der Waals Density Functionals as an Additive Correction: An Extensive Analysis with Special Emphasis on the B97M-V and ωB97M-V Approaches. *J. Chem. Theory Comput.* **2018**, *14* (11), 5725−5738.
(35) Grimme, S.; Antony, J.; Ehrlich, S.; Krieg, H. A consistent and accurate ab initio parametrization of density functional dispersion correction (DFT-D) for the 94 elements H-Pu. *J. Chem. Phys.* **2010**, *132*, 15.
(36) Lee, K.; Murray, E. D.; Kong, L.; Lundqvist, B. I.; Langreth, D. C. Higher-accuracy van der Waals density functional. *Phys. Rev. B* **2010**, *82* (8), 081101.
(37) Feyereisen, M.; Fitzgerald, G.; Komornicki, A. Use of approximate integrals in ab initio theory. An application in MP2 energy calculations. *Chem. Phys. Lett.* **1993**, *208* (5), 359−363.
(38) Riplinger, C.; Neese, F. An efficient and near linear scaling pair natural orbital based local coupled cluster method. *J. Chem. Phys.* **2013**, *138*, 3.
(39) Planas, N.; Mondloch, J. E.; Tussupbayev, S.; Borycz, J.; Gagliardi, L.; Hupp, J. T.; Farha, O. K.; Cramer, C. J. Defining the Proton Topology of the Zr6-Based Metal−Organic Framework NU-1000. *J. Phys. Chem. Lett.* **2014**, *5* (21), 3716−3723.
(40) Kozuch, S.; Shaik, S. How to Conceptualize Catalytic Cycles? The Energetic Span Model. *Acc. Chem. Res.* **2011**, *44* (2), 101−110.
(41) Sapienza, N. S.; Knight, K. N.; Albrahim, M.; Yousuf, M. R.; Karim, A. M.; Morris, J. R. Autocatalysis through the Generation of Water during Methanol Oxidation over a Titania-Supported Platinum Catalyst. *ACS Catal.* **2023**, *13* (15), 9997−10006.
(42) Tesvara, C.; Karwacki, C. J.; Sautet, P. Decomposition of the Toxic Nerve Agent Sarin on Oxygen Vacancy Sites of Rutile TiO2(110). *J. Phys. Chem. C* **2023**, *127* (17), 8006−8015.
(43) Tesvara, C.; Walenta, C.; Sautet, P. Oxidative decomposition of dimethyl methylphosphonate on rutile TiO2(110): the role of oxygen vacancies. *Phys. Chem. Chem. Phys.* **2022**, *24* (38), 23402−23419.
(44) Bermudez, V. M. Effect of Humidity on the Interaction of Dimethyl Methylphosphonate (DMMP) Vapor with SiO2 and Al2O3 Surfaces, Studied Using Infrared Attenuated Total Reflection Spectroscopy. *Langmuir* **2010**, *26* (23), 18144−18154.
(45) Bermudez, V. M. Computational Study of Environmental Effects in the Adsorption of DMMP, Sarin, and VX on γ-Al2O3: Photolysis and Surface Hydroxylation. *J. Phys. Chem. C* **2009**, *113* (5), 1917−1930.
(46) Choudhuri, I.; Ye, J.; Truhlar, D. G. Computational quantum chemistry of metal−organic frameworks.*Chem. Phys. Rev.*, **2023**; Vol. *43*
(47) Klet, R. C.; Wang, T. C.; Fernandez, L. E.; Truhlar, D. G.; Hupp, J. T.; Farha, O. K. Synthetic access to atomically dispersed metals in metal−organic frameworks via a combined atomic-layer-deposition-in-MOF and metal-exchange approach. *Chem. Mater.* **2016**, *28* (4), 1213−1219.
(48) Zhao, Y.; Truhlar, D. G. Applications and validations of the Minnesota density functionals. *Chem. Phys. Lett.* **2011**, *502* (1−3), 1−13.
(49) Li, Z.; Schweitzer, N. M.; League, A. B.; Bernales, V.; Peters, A. W.; Getsoian, A. B.; Wang, T. C.; Miller, J. T.; Vjunov, A.; Fulton, J. L. Sintering-resistant single-site nickel catalyst supported by metal−organic framework. *J. Am. Chem. Soc.* **2016**, *138* (6), 1977−1982.
(50) Kim, I. S.; Borycz, J.; Platero-Prats, A. E.; Tussupbayev, S.; Wang, T. C.; Farha, O. K.; Hupp, J. T.; Gagliardi, L.; Chapman, K. W.; Cramer, C. J.; Martinson, A. B. Targeted single-site MOF node modification: trivalent metal loading via atomic layer deposition. *Chem. Mater.* **2015**, *27* (13), 4772−4778.
(51) Costanzi, S.; Machado, J.-H.; Mitchell, M. Nerve Agents: What They Are, How They Work, How to Counter Them. *ACS Chem. Neurosci.* **2018**, *9* (5), 873−885.

https://doi.org/10.1021/acs.jpcc.4c01312
J. Phys. Chem. C 2024, 128, 8983−8992